PCCP

ROYAL SOCIETY OF CHEMISTRY

PAPER

View Article Online
View Journal

Cite this: DOI: 10.1039/d0cp06150f

Solution structure of a europium–nicotianamine complex supports that phytosiderophores bind lanthanides†

Danil S. Kaliakin, ‡[a] Josiane A. Sobrinho, ‡[b] Jorge H. S. K. Monteiro, [b] Ana de Bettencourt-Dias [b] and David C. Cantu *[a]

Received 26th November 2020,
Accepted 1st February 2021

DOI: 10.1039/d0cp06150f

rsc.li/pccp

We report the solution structure of a europium-nicotianamine complex predicted from *ab initio* molecular dynamics simulations with density functional theory. Emission and excitation spectroscopy show that the Eu^{3+} coordination environment changes in the presence of nicotianamine, suggesting complex formation, such as what is seen for the Eu^{3+}–nicotianamine complex structure predicted from computation. We modeled Eu^{3+}–ligand complexes with explicit water molecules in periodic boxes, effectively simulating the solution phase. Our simulations consider possible chemical events (*e.g.* coordination bond formation, protonation state changes, charge transfers), as well as ligand flexibility and solvent rearrangements. Our computational approach correctly predicts the solution structure of a Eu^{3+}–ethylenediaminetetraacetic acid complex within 0.05 Å of experimentally measured values, backing the fidelity of the predicted solution structure of the Eu^{3+}–nicotianamine complex. Emission and excitation spectroscopy measurements were also performed on the well-known Eu^{3+}–ethylenediaminetetraacetic acid complex to validate our experimental methods. The electronic structure of the Eu^{3+}–nicotianamine complex is analyzed to describe the complexes in greater detail. Nicotianamine is a metabolic precursor of, and structurally very similar to, phytosiderophores, which are responsible for the uptake of metals in plants. Although knowledge that nicotianamine binds europium does not determine how plants uptake rare earths from the environment, it strongly supports that phytosiderophores bind lanthanides.

I. Introduction

The remarkable and unique characteristics of electronic states of lanthanide (Ln) complexes originating from partially filled 4f-electron shells, and their extremely localized nature, make studies of their compounds a very active area of research.[1–18] Lanthanides are used in a multitude of high-tech applications,[3] including luminescence, which arises from the photophysical properties of Ln–ligand complexes.[5–10,12–17] Ln–ligand complexes are also relevant to medical imaging and therapeutics.[4] In comparison, the role of lanthanides in naturally-occurring biological systems has been somewhat overlooked.

Lanthanides have been detected in plants and their roots,[19–22] however plant uptake and transport of rare earth elements remains largely unknown.[21,23,24] It is not clear whether accumulation happens through Ca or Fe uptake pathways involving the broad-spectrum metallophore nicotianamine (NA), or if Ln intake and accumulation are the result of production of lanthanophores by bacteria residing in the phyllosphere.[21,25] Despite limited mechanistic knowledge, rare earth phytoextraction[26–28] is an active research area, for environmental remediation[29] and/or lanthanide recovery.[30,31] Moreover, a number of studies show that the Ln elements affect the growth and development of agriculturally important crops.[19,20,32]

Until recently, lanthanides were not considered as essential elements of biological systems and Ln-incorporated enzymes were viewed as useful, yet mainly artificial, systems.[3,25,33] This perspective changed with the discovery of lanthanides in bacterial methanol dehydrogenases[34–36] and resolving the role of lanthanides in enzymatic mechanisms.[37] Interestingly, Liu *et al.*[38] demonstrated that Rubisco,[39] an enzyme crucial for photosynthetic CO_2 fixation in higher plants,[38,40] binds cerium,

[a] *Department of Chemical and Materials Engineering, University of Nevada, Reno, NV, 89557, USA. E-mail: dcantu@unr.edu*
[b] *Department of Chemistry, University of Nevada, Reno, NV 89557, USA*

† Electronic supplementary information (ESI) available: Atomic Cartesian coordinates (Å) of the PBE/LnPP1 GTH optimized structures of $[Eu^{3+}–EDTA^{4-}\cdot(H_2O)_3]^-$, $[Eu^{3+}–NA\cdot(H_2O)_3]^{3+}$, $[Eu^{3+}–NA\cdot(H_2O)_4]^{3+}$ and $[Eu^{3+}–NA\cdot(H_2O)_5]^{3+}$ complexes. Potential energy plots for AIMD trajectories. Coordination bond lengths of the $[Eu^{3+}–EDTA^{4-}\cdot(H_2O)_3]^-$, $[Eu^{3+}–NA\cdot(H_2O)_3]^{3+}$, and $[Eu^{3+}–NA\cdot(H_2O)_4]^{3+}$ complexes along the AIMD trajectories. $[Eu^{3+}–EDTA^{4-}\cdot(H_2O)_3]^-$ complex molecular orbitals. Complex binding energies. See DOI: 10.1039/d0cp06150f

‡ Equal contribution.

which shows Ln^{3+}-binding capability of compounds native to plants.

Low-molecular weight chelators with functional carboxy-, amino- and hydroxy-groups facilitating metal coordination in bacteria and plants are classified as siderophores and phytosiderophores, respectively.[41–44] When it comes to understanding the role of these compounds in the metabolism of lanthanides in plants, NA, a metallophore naturally occurring in higher plants,[41,45] is of particular interest. NA is structurally very similar to phytosiderophores, and it is a precursor in phytosiderophores biosynthetic pathways,[41] which makes it an ideal model system.

Apart from its importance for understanding the role of lanthanides in plant metabolic transformations and phytoextraction, elucidating the solution structure of Ln^{3+} complexes with NA could potentially contribute to the development of ligands for Ln extraction. Siderophores have been shown to bind Ln^{3+} ions[46–48] with a pH-sensitive binding behavior.[47,49] Like siderophores, the molecular structures of phytosiderophores are highly susceptible to changes in protonation states,[41,50–52] but, unlike siderophores, their ability to bind Ln^{3+} ions has not been elucidated.

Lanthanide coordination is affected by a number of factors in the surrounding environment, such as flexibility and protonation state of the bound ligand.[53–57] Due to the high coordination number of Ln^{3+} ions, in addition to the ligand, water (or solvent) molecules will coordinate as well. Thus, the solution structure of Ln^{3+}–ligand complexes and their stabilities strongly depend on the molecular structure of their coordination spheres, which include ligand and solvent molecules.[58]

Resolving the solution structure of Ln^{3+}–ligand complexes is a nontrivial task due to their highly dynamical nature. To do so computationally, in atomic resolution, requires the use of density functional theory (DFT) and *ab initio* molecular dynamics (AIMD) to simulate the breakage and formation of chemical bonds (*e.g.* coordination bonds, protonation state changes) simultaneously considering ligand flexibility and solvent rearrangements. Additionally, simulating solution structures (*i.e.* condensed phase) requires including explicit solvent molecules, and treating the system periodically in repeating unit cells. An accurate periodic treatment of solute–solvent systems requires periodic boxes of sufficient size, which makes such all-electron AIMD simulations computationally out of reach, thus requiring DFT.

The employment of relativistic, norm-conserving, separable, dual-space Gaussian-type pseudopotential protocol of Goedecker, Teter, and Hutter (GTH)[59–61] in a mixed Gaussian-plane wave scheme[62] has proved to be an effective and efficient way to perform AIMD simulations of larger systems (>500 atoms)[63,64] and with longer trajectories (>10 ps),[63,65] significantly reducing the computational cost of such simulations. Until recently, accurate GTH pseudopotentials and basis sets for the lanthanides, besides cerium,[66,67] were lacking. This prevented performing larger-scale DFT and AIMD simulations of lanthanide-containing systems in the condensed phase or solid state. Our previous work bridged this critical gap by producing LnPP1: a full set of well-benchmarked pseudopotentials along with the corresponding basis sets within GTH protocol specifically optimized for GGA PBE[68] calculations of lanthanide-containing systems.[69] Despite the fact that other types of lanthanide pseudopotentials (*i.e.* effective core potentials) and basis sets were previously reported,[70–76] these were employed in electronic structure calculations with lanthanide systems containing less than $\sim$100 atoms.[77,78] Thus, simulating the solution structure of lanthanide–ligand complexes, with molecular dynamics sampling to explicitly include solvent rearrangement and ligand flexibility, was not possible until very recently. Our LnPP1 complete set of pseudopotentials and accompanying basis sets enabled us to perform DFT calculations and AIMD simulations of lanthanide–ligand complexes in explicit water boxes in periodic conditions (system >500 atoms) in the present paper.

This work pursued two goals: (i) demonstrate that our pseudopotentials and basis sets (LnPP1) with AIMD simulations can predict the structures of lanthanide complexes in solution and, (ii) elucidate the molecular and electronic structure of Eu^{3+}–nicotianamine complexes in aqueous solution. Our previous work[69] demonstrated the accuracy of our LnPP1 pseudopotentials and basis sets to replicate Ln reactivity (*e.g.* oxidation reactions, heats of formation, ionization potentials). This work shows that our pseudopotentials and basis sets with AIMD simulations replicate the solution structure of lanthanide–ligand complexes, by correctly (within 0.05 Å) predicting the structure of a complex whose structure is known (Eu^{3+}–ethylenediaminetetraacetic acid [EDTA]).[79,80] Upon validation of the computational approach, we predict the structure of Eu^{3+}–nicotianamine complexes in solution: this work describes their molecular structures (*e.g.* ligand conformation, water molecule inclusion, coordination bond geometry) and electronic structure (*e.g.* molecular orbitals). Further, with excitation and emission spectroscopy, we measured an *in vitro* change in Eu^{3+} coordination upon coming in contact with nicotianamine, supporting the formation of a Eu^{3+}–nicotianamine complex.

II. Methods

II.A. Computational details

II.A.1. *Ab initio* molecular dynamics simulations. All geometry optimizations and AIMD simulations were performed in cubic periodic boxes 17.5 Å in length within the PBE/LnPP1 GTH level of theory,[68,69] as implemented in the CP2K package.[81] The PBE functional has been well-tested for both water[82,83] and lanthanides.[84,85] Core electrons were modeled with norm-conserving GTH pseudopotentials, while valence electrons, including f electrons, were treated with polarizable double-zeta quality basis sets.[86] We used our recently developed LnPP1 pseudopotentials and basis sets for europium.[69] The long-range electrostatics terms were calculated with an additional plane wave basis set with a 500 Ry cutoff. Grimme's corrections[87] were used to account for van der Waals interactions with a 6.0 Å radius.

All AIMD simulations were done at fixed volume and temperature (*NVT* ensemble), with a 1.0 fs or 0.5 fs time step. A 1.0 fs time step is sufficient, although initially we used a 0.5 fs time step. Initial complex structures were placed in the center of the periodic box and solvated with water molecules. We used the following protocol to obtain optimized aqueous structures of the Eu^{3+}–ligand complexes: we initially performed 5 ps of *NVT* AIMD simulations at 363 K, which were followed by a slow annealing to 0 K with rescaling factor for annealing velocities equal to 0.997, and final geometries optimizations. Starting from the optimized geometries, production AIMD simulations of Eu^{3+}–ligand complexes were performed at 300 K for >10 ps trajectories. The analysis of radial distribution functions (RDFs) and coordination numbers (CNs) of the studied systems was done for equilibrated parts of the trajectories that corresponded to at least ~10 ps. Potential energy plots along the production AIMD trajectories appear in the ESI,† Fig. S1. All of the models containing Eu^{3+} had a septet spin multiplicity.

We modelled the Eu^{3+}–EDTA complex with the EDTA protonation state corresponding to pH 11 (four carboxylate sites and two amine sites deprotonated) resulting in $EDTA^{4-}$. The EDTA protonation states were chosen to correspond to pH 11 to be able to directly compare with the published Eu^{3+}–EDTA complex structure.[79,80] Our model periodic unit cell contained 574 atoms, which included 33 atoms representing the $[Eu^{3+}$–$EDTA^{4-}]^{-}$ complex, 180 explicit water molecules, and 1 Na^{+} counter ion, allowing for the overall neutral charge of the periodic unit cell (Fig. 1a). Since the structure of the $[Eu^{3+}$–$EDTA^{4-}]^{-}$ complex in solution is known, we initially constructed the complex with the known structure, and subjected it to the AIMD protocol described.

We modelled the Eu^{3+}–NA complex with NA as a zwitterion (three carboxylate sites deprotonated and three amine sites protonated) resulting in a net uncharged ligand. NA has a zwitterionic protonation state from pH ~ 3.2 to pH ~ 7.7.[41,88] We modelled NA as a zwitterion to directly compare with our experiments performed at pH ~ 5. Our model periodic unit cell contained 586 atoms, which included 43 atoms corresponding to the $[Eu^{3+}$–$NA]^{3+}$ complex, 180 explicit water molecules, and three Cl^{-} counter ions allowing for the overall neutral charge of the unit cell (Fig. 1b). In order to account for different possible conformations of the $[Eu^{3+}$–$NA]^{3+}$ complex structure, we independently constructed this system with four different initial structures: (i) structure with all three NA–COO^{-} groups having bidentate binding to Eu^{3+}, (ii) structure with two bidentate NA–COO^{-} groups binding to Eu^{3+} and one monodentate, (iii) structure with one bidentate NA–COO^{-} group and two monodentate, and (iv) structure with all three NA–COO^{-} groups having monodentate binding to Eu^{3+}. All four initial structures were independently subjected to the AIMD protocol described. Due to the large number of degrees of freedom in explicitly solvated $[Eu^{3+}$–$NA]^{3+}$ complexes, we performed additional 10 ps AIMD simulations at 363 K, to verify that the complexes remain in the binding conformation.

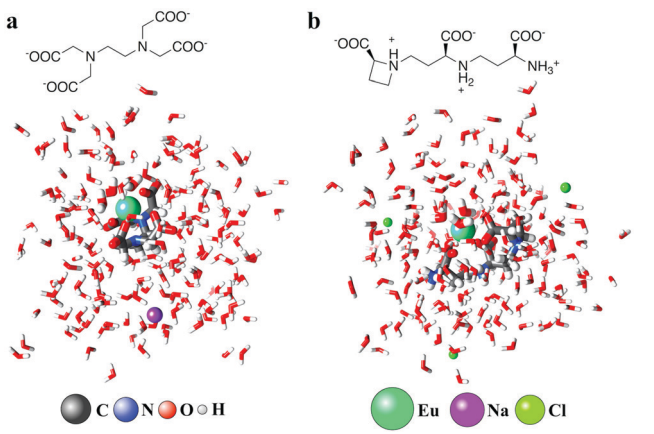

Fig. 1 Unit cells used in periodic simulations. (a) Unit cell of the Eu^{3+}–$EDTA^{4-}$ model system. (b) Unit cell of the Eu^{3+}–NA model system. Drawings of $EDTA^{4-}$ and NA shown.

II.A.2. Electronic structure analysis. We studied the electronic structure of the optimized complex structures in further detail by analyzing the molecular orbitals (MOs) of Eu^{3+}–ligand complex coordination bonds. Starting from the optimized (annealing plus geometry optimization) solution structures of our Eu^{3+}–ligand complexes with explicit water molecules, we extracted the atomic coordinates of the Eu^{3+}–ligand complexes, including water molecules that are directly coordinated with the Eu^{3+} ion, and performed single point energy calculations in the ORCA software package[89–91] with the M06 functional,[92] a relativistic second order Douglas–Kroll–Hess (DKH2) Hamiltonian,[93,94] and segmented all-electron relativistically-contracted (SARC) basis set[95] for Eu. The def2-TZVPP basis set[96] was used for other chemical elements within the model systems.[97] All single point energy calculations were done with an implicit water solvent model (conductor-like polarizable continuum model).[98] The M06 functional was chosen due to it is general reliability in prediction of thermodynamic properties,[99] particularly in case of lanthanide complexes.[84,85] The efficiency of DKH2 and SARC basis set in prediction of electronic properties of lanthanide was demonstrated in previous studies.[100–102] All the ORCA calculations were done with the resolution of identity chain of sphere (RIJCOSX)[103] to improve the calculations efficiency, with "Grid7" and "GridX7" grids. Multiplicities, particularly septet for Eu^{3+} and Eu^{3+}–ligand complexes, were verified by looking at spin contamination; we obtained very low deviation values (~0.003 for Eu^{3+}, ~0.01 for Eu^{3+}–ligand complexes), indicating no significant contamination.

All geometry optimizations were done in the solution phase (*i.e.*, with explicit water molecules, periodic conditions) with CP2K, and we extracted the coordinates of only the molecules (ligand and water) coordinated with Eu^{3+} ions to analyze the electronic structure of the complexes. We did not further optimize the structures with implicit solvent to directly probe the electronic properties of structures that correspond to aqueous solution at room temperature.

II.B. Experimental details

II.B.1. Complex and solution preparation. $EuCl_3{\cdot}(H_2O)_6$ was purchased from Strem Chemicals and dried under reduced

pressure and heating for at least 12 hours. NA was purchased from Toronto Research Chemicals and used as received. Eu^{3+}–NA complexes were prepared by mixing NA and $EuCl_3$ in a 1 : 1 stoichiometry, in water, followed by stirring at room temperature for 4 h. The pH of the complex solution was ~5.5, and no precipitation was observed. Solutions with concentrations 1×10^{-4} M were prepared for photophysical studies.

We prepared Eu^{3+}–EDTA complexes to verify our experimental methods and support our results with Eu^{3+}–NA complexes. Eu^{3+}–EDTA complexes were formed by mixing Na_2–EDTA and dry $EuCl_3$ in a 1 : 1 stoichiometry in water. The pH was adjusted to ~2.9, with HCl(aq), or pH ~ 7.1, with $Na_2HPO_4/NaHPO_4$ buffer. At pH ~ 2.9 the resulting complex is $[Eu^{3+}\text{–}EDTA^{2-}\cdot(H_2O)_n]^+$ complex, and at pH ~ 7.1 it is $[Eu^{3+}\text{–}EDTA^{3-}\cdot(H_2O)_n]$.

II.B.2. Photophysical studies. The photoluminescence data were obtained on a Fluorolog-3 spectrofluorimeter (Horiba FL3-22-iHR550), with a 1200 grooves per mm excitation monochromator with gratings blazed at 330 nm and a 1200 grooves per mm emission monochromator with gratings blazed at 500 nm. An ozone-free 450 W xenon lamp (Ushio) was used as a radiation source. The emission spectra were measured in the range 550–725 nm using a Hamamatsu 928P detector. All emission spectra were corrected for instrumental function.

III. Results and discussion

III.A. Our computational approach replicates the known Eu^{3+}–EDTA complex structure

Our optimized $[Eu^{3+}\text{–}EDTA^{4-}\cdot(H_2O)_3]^-$ complex structure matches the structure previously obtained with X-ray crystallography,[79] where the Eu^{3+} ion is 9-coordinate with 4 oxygen atoms from the coordinated monodentate carboxylates, two nitrogen atoms from the coordinated amines, and 3 oxygen atoms from the coordinated water molecules. This confirms that our Eu pseudopotential and basis set, as well as the AIMD protocol described, accurately replicate the structure of the $[Eu^{3+}\text{–}EDTA^{4-}\cdot(H_2O)_3]^-$ complex in solution, in which the EDTA protonation states correspond to pH 11.

Fig. 2 shows the resulting optimized structure, with coordination sites 1, 2, and 3 corresponding to water molecules, coordination sites 4, 5, 8 and 9 to monodentate $-COO^-$ groups, and coordination sites 6 and 7 to amines. The atomic Cartesian coordinates of the optimized $[Eu^{3+}\text{–}EDTA^{4-}\cdot(H_2O)_3]^-$ structure are reported in the ESI.†

From ~10 ps of equilibrated AIMD simulations of the $[Eu^{3+}\text{–}EDTA^{4-}\cdot(H_2O)_3]^-$ complex we calculated Eu–O (Fig. 3a), Eu–N (Fig. 3b), and Eu–C (Fig. 3c) RDFs and CNs to quantify meaningful solution structures that account for ligand and solvent fluctuations, as well as to directly compare with reported Eu–O, Eu–N, and Eu–C distances measured with extended X-ray absorption fine structure (EXAFS) spectroscopy. Potential energy plot for corresponding AIMD trajectory is reported in Fig. S1a (ESI†), and Eu–N and Eu–O bond lengths along the AIMD simulations are plotted in Fig. S2–S5 in the ESI.†

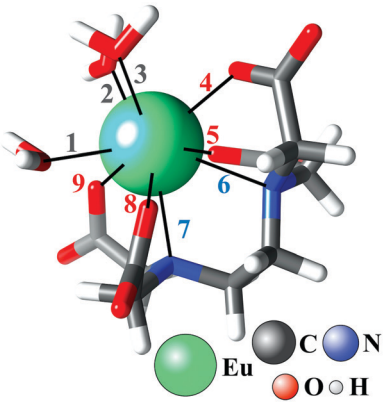

Fig. 2 Geometry of the PBE/LnPP1 GTH optimized structure of the $[Eu^{3+}\text{–}EDTA^{4-}\cdot(H_2O)_3]^-$ complex. Black solid lines connected to the Eu atom demonstrate the positions of coordination sites. Coordination sites numbers colored in dark grey, red and blue represent water, monodentate $-COO^-$, and nitrogen atom coordination sites, respectively. Only water molecules coordinated to Eu^{3+} are shown for clarity.

The RDFs calculated for the $[Eu^{3+}\text{–}EDTA^{4-}\cdot(H_2O)_3]^-$ complex, shown in Fig. 3, have maxima at 2.46 Å for the Eu–O pair, 2.77 Å for the Eu–N pair, and 3.35 Å for the Eu–C pair. The oxygen and nitrogen atoms directly coordinated to the Eu^{3+} ion correspond to the first coordination sphere, with the ligand carbon atom slightly further away. In Fig. 3a (Eu–O RDF) a smaller peak at 4.57 Å is shown, which corresponds to the second coordination sphere, which is the solvent (water) shell around the $[Eu^{3+}\text{–}EDTA^{4-}\cdot(H_2O)_3]^-$ complex. The Eu–O and Eu–N RDFs we calculated from AIMD simulations closely match the previously EXAFS-measured Eu–O and Eu–N pair distances, reported as 2.41 Å and 2.76 Å, respectively.[80] Thus, the largest deviation between the experimentally measured radial pair distances and our calculated RDFs from AIMD simulations does not exceed 0.05 Å, demonstrating the reliability and accuracy of PBE/LnPP1 GTH AIMD simulations to replicate solution structures of Ln^{3+}–ligand complexes.

III.B. The solution structure of Eu^{3+}–nicotianamine complexes resolved with *ab initio* molecular dynamics

In order to account for different possible conformations of $[Eu^{3+}\text{–}NA]^{3+}$ complexes, we performed AIMD simulations of this system with four different initial conformations, as described in section III.A.1. The complex with all three NA–COO^- groups having bidentate binding to Eu^{3+} did not remain in that binding conformation during the AIMD simulation; a bidentate carboxylate became monodentate. We found three $[Eu^{3+}\text{–}NA]^{3+}$ complex structures that kept their conformation in the AIMD simulations, indicating that these conformations are likely to be observed at room temperature in solution. One structure includes three water molecules directly coordinated to the Eu^{3+} ion (Fig. 4a), in which the Eu^{3+} ion is coordinated to two carboxylates in a bidentate conformation and one in a monodentate conformation. In the $[Eu^{3+}\text{–}NA\cdot(H_2O)_3]^{3+}$ complex structure (Fig. 4a), coordination sites 1, 2, and 3 correspond to water molecules, coordination sites 4, 5, 7 and 8 to bidentate $-COO^-$

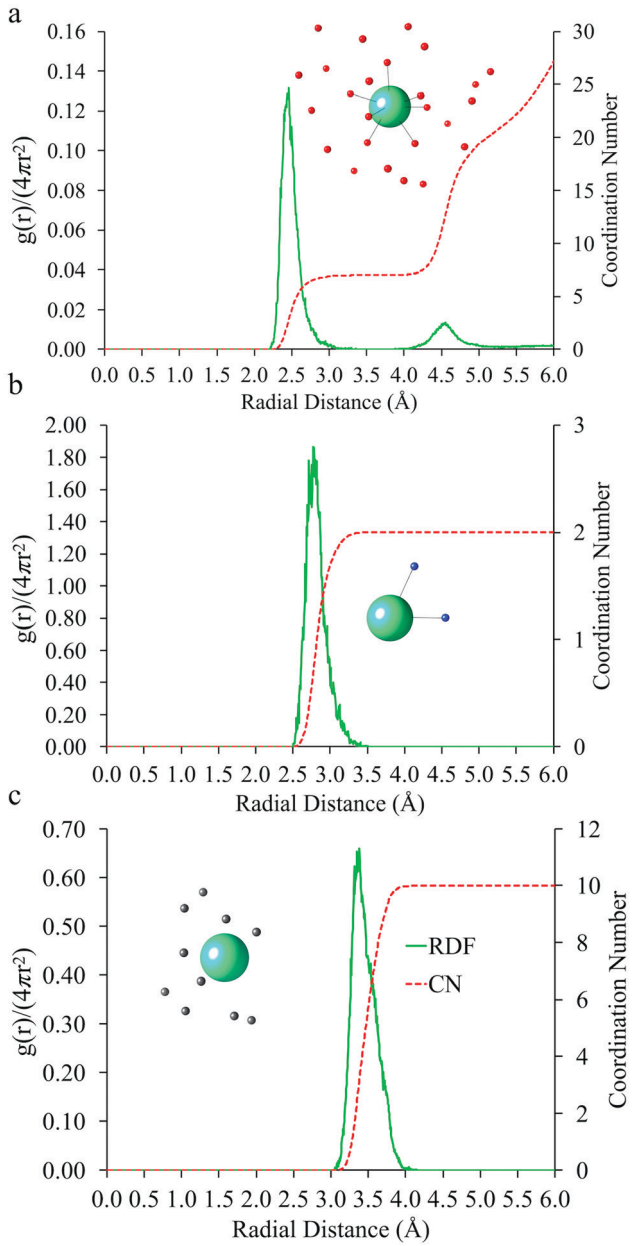

Fig. 3 Radial distribution functions (RDF) and coordination numbers (CN) of the $[Eu^{3+}–EDTA^{4-}·(H_2O)_3]^-$ complex from the equilibrated AIMD trajectory for (a) Eu–O atoms, (b) Eu–N atoms, and (c) Eu–C atoms. Panels inside the graphs represent the distribution of the corresponding atoms in equilibrated and consecutively optimized structures. Solid lines connecting Eu with surrounding atoms represent coordinated atoms.

groups, and coordination site 6 to a monodentate $–COO^-$ group. The second structure has four water molecules directly coordinated to the Eu^{3+} ion (Fig. 4b), in which the Eu^{3+} ion is coordinated to one carboxylate in a bidentate and two in a monodentate fashion. In the $[Eu^{3+}–NA·(H_2O)_4]^{3+}$ complex structure (Fig. 4b), coordination sites 1, 2, 3 and 4 correspond to water molecules, coordination sites 5 and 7 to the bidentate $–COO^-$ group, and coordination sites 6 and 8 two each monodentate $–COO^-$ group. The third structure has five water molecules directly coordinated to the Eu^{3+} ion (Fig. 4c), in which the Eu^{3+} ion is coordinated to the three carboxylate groups in a monodentate way. In the $[Eu^{3+}–NA·(H_2O)_5]^{3+}$ complex structure (Fig. 4c), coordination sites 2, 3, 4, 5 and 8 correspond to water molecules, and coordination sites 1, 6 and 7 to each monodentate $–COO^-$ group. The atomic Cartesian coordinates of the three complexes appear in the ESI.† Unlike the 9-coordinate $[Eu^{3+}–EDTA^{4-}·(H_2O)_3]^-$ complex, all Eu–NA complexes are 8-coordinate.

Starting from the optimized complex structures, we calculated the RDFs and CNs for the three complexes using ~10 ps of equilibrated AIMD trajectories. Fig. 5 shows the Eu–O, Eu–N, and Eu–C RDFs and CNs of the $[Eu^{3+}–NA·(H_2O)_3]^{3+}$, $[Eu^{3+}–NA·(H_2O)_4]^{3+}$, and $[Eu^{3+}–NA·(H_2O)_5]^{3+}$ complexes, respectively. Potential energy plots of the corresponding AIMD trajectories are reported in Fig. S1 (ESI†). Eu–N and Eu–O bond lengths along the AIMD simulations are plotted in Fig. S2–S5 in the ESI.†

Table 1 shows the distances of the RDFs peaks, extracted from Fig. 3 and 5 to compare the three $[Eu^{3+}–NA·(H_2O)_n]^{3+}$ complex structures with each other and with the known $[Eu^{3+}–EDTA^{4-}·(H_2O)_3]^-$ structure. The three 8-coordinate $[Eu^{3+}–NA·(H_2O)_n]^{3+}$ complex structures have very similar Eu–O RDF profiles, however, there are changes in the Eu–N and Eu–C profiles. This means that the change in the binding mode (monodentate or bidentate) of carboxylate groups in $[Eu^{3+}–NA·(H_2O)_n]^{3+}$ complexes resulted in different conformations of the entire complex due to ligand flexibility in solution.

The $[Eu^{3+}–EDTA^{4-}·(H_2O)_3]^-$ complex has its coordinating oxygen atoms ~0.10 Å further than all three $[Eu^{3+}–NA·(H_2O)_n]^{3+}$ complexes, perhaps due to the fact that the complex with EDTA includes N atoms in the first coordination sphere. All complexes share similar 2nd (~4.5 Å) sphere Eu–O distances. While the $[Eu^{3+}–EDTA^{4-}·(H_2O)_3]^-$ complex includes nitrogen atoms (amine sites) in its first coordination sphere, all $[Eu^{3+}–NA·(H_2O)_n]^{3+}$ complexes have only oxygen atoms in their first solvation shell. This is evidenced in the Eu–N RDF plots, which show a single peak for $[Eu^{3+}–EDTA^{4-}·(H_2O)_3]^-$ ~ 2.8 Å (Fig. 3), while more disordered peaks are seen for the $[Eu^{3+}–NA·(H_2O)_n]^{3+}$ complexes at distances >4 Å (Fig. 5). This means that the amine NA sites are on the "outside" of the first coordination sphere of the Eu–NA complexes, and are in contact with solvent molecules, unlike the $[Eu^{3+}–EDTA^{4-}·(H_2O)_3]^-$ complex structure where most ligand heteroatoms are coordinated to the Eu^{3+} ion, which has implications toward lanthanide–ligand complex solubility. Similarly, the Eu-C RDF plots of the $[Eu^{3+}–NA·(H_2O)_n]^{3+}$ complexes are more disordered than the single Eu–C peak for $[Eu^{3+}–EDTA^{4-}·(H_2O)_3]^-$, which implies that the $[Eu^{3+}–EDTA^{4-}·(H_2O)_3]^-$ complex is more rigid than the $[Eu^{3+}–NA·(H_2O)_n]^{3+}$ complexes, which has implications toward complex stability.

III.C. Eu^{3+} coordination changes in the presence of nicotianamine

Ln^{3+} ions emit light,[7] a property which arises from transitions within the 4f orbitals and that we will use to determine Ln^{3+}–ligand complex formation. The core nature of the 4f orbitals,

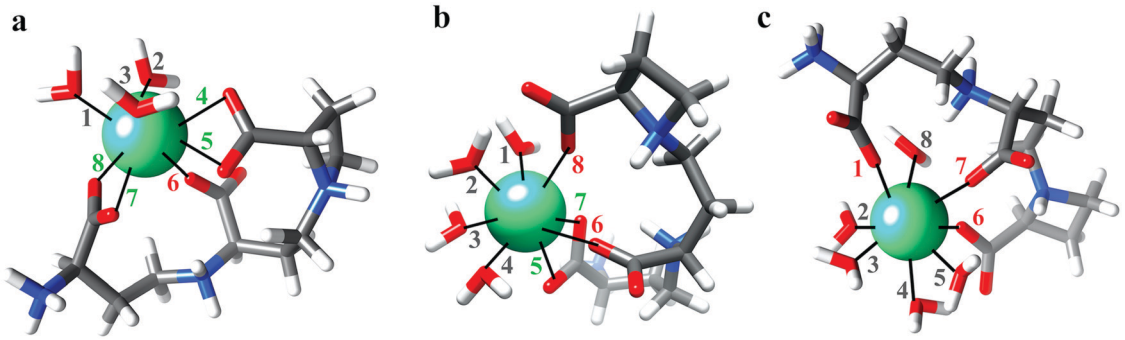

Fig. 4 PBE/LnPP1 GTH geometry optimized structure of the (a) $[Eu^{3+}–NA·(H_2O)_3]^{3+}$, (b) $[Eu^{3+}–NA·(H_2O)_4]^{3+}$, and (c) $[Eu^{3+}–NA·(H_2O)_5]^{3+}$ complexes. Black solid lines connected to Eu atom demonstrate the positions of coordination sites. Numbers colored in dark grey, red and green represent water, monodentate $–COO^-$, and bidentate $–COO^-$ coordination sites, respectively. Only water molecules coordinated to Eu^{3+} shown for clarity. The same color scheme as in Fig. 2 is used.

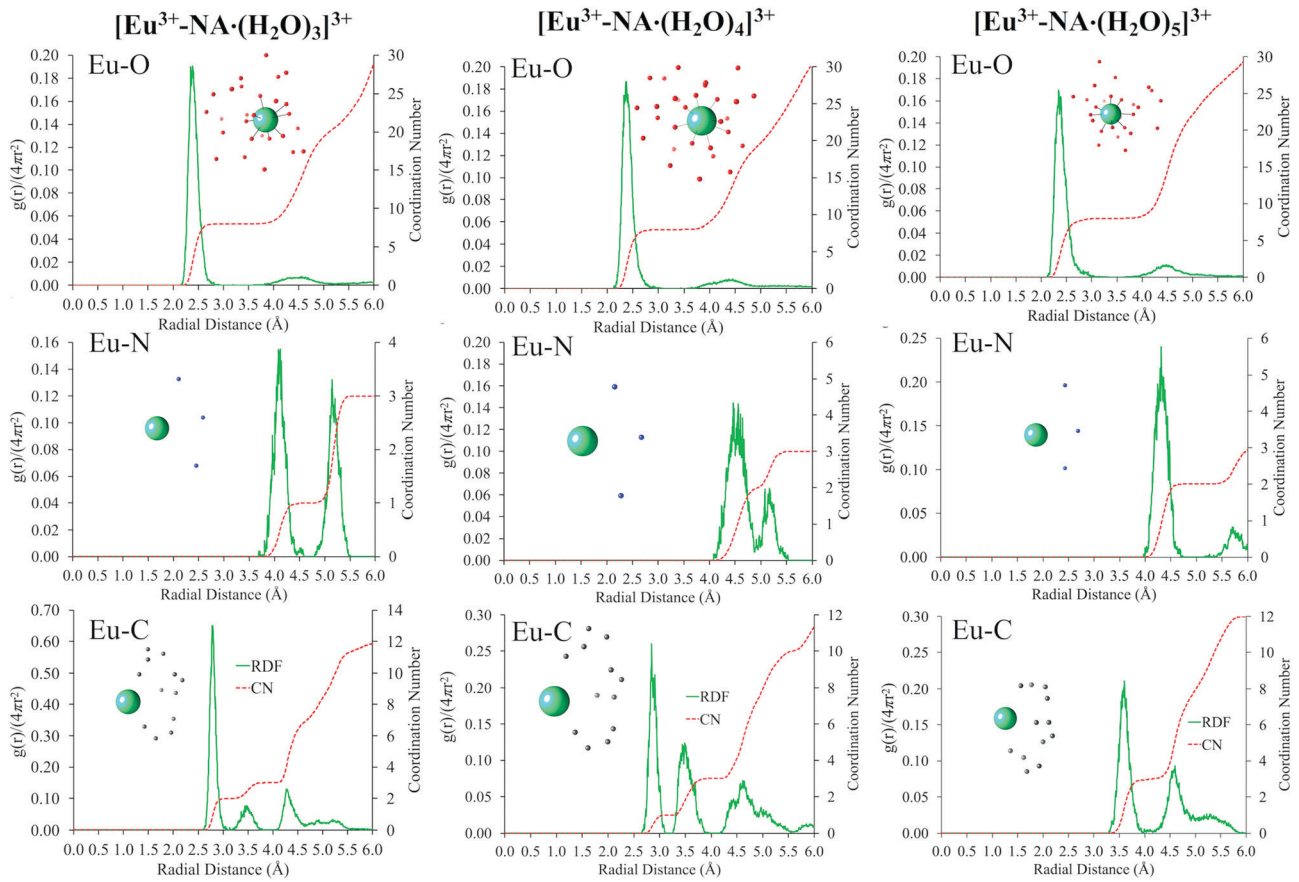

Fig. 5 Radial distribution functions (RDF) and coordination numbers (CN) of the $[Eu^{3+}–NA·(H_2O)_3]^{3+}$ complex (left column), $[Eu^{3+}–NA·(H_2O)_4]^{3+}$ complex (middle column), and $[Eu^{3+}–NA·(H_2O)_5]^{3+}$ complex (right column) from their equilibrated AIMD trajectories for Eu–O atoms (top row), Eu–N atoms (middle row), and Eu–C atoms (bottom row). Panels inside the graphs represent the distribution of the corresponding atoms in equilibrated and consecutively optimized structures. Solid lines connecting Eu atom and surrounding atoms represent coordinated atoms.

which are shielded from the environment of Ln^{3+} ions by the filled 5s and 5p orbitals,[104] leaves them mostly unaffected by the coordination environment; it results in the formation of mostly ionic bonds, and does not significantly affect their energy and shape. Thus, f–f transitions are characteristic of each ion. In addition, f–f transitions are forbidden by the parity rule. However, the symmetry of the coordination environment partially lifts the restrictions, which enables the use of emission spectroscopy to characterize the symmetry of the coordination sphere of Eu^{3+}.[12] Excitation and emission spectra are easily interpreted for the Eu^{3+} ion, because it has an electronic structure in which the excited- and ground-state energy level

Table 1 Peak distances (Å) of the RDFs from AIMD simulations for $[Eu^{3+}–EDTA^{4-}·(H_2O)_3]^-$ and $[Eu^{3+}–Na·(H_2O)_n]^{3+}$ complexes. The peaks absent in RDFs marked with a "—"

	$[Eu^{3+}–EDTA^{4-}·(H_2O)_3]^-$			$[Eu^{3+}–NA·(H_2O)_3]^{3+}$			$[Eu^{3+}–NA·(H_2O)_4]^{3+}$			$[Eu^{3+}–NA·(H_2O)_5]^{3+}$		
	1st	2nd	3rd	1st	2nd	3rd	1st	2nd	3rd	1st	2nd	3rd
Eu–O	2.46	4.57	—	2.38	4.57	—	2.38	4.45	—	2.39	4.53	—
Eu–N	2.78	—	—	4.08	5.14	—	4.46	5.16	—	4.29	5.71	—
Eu–C	3.38	—	—	2.79	3.49	4.27	2.84	3.49	4.65	3.60	4.60	—

multiplets do not overlap,[105] allowing for simple spectral interpretation. The fine structure in the emission spectra of Eu^{3+} complexes is directly related to the coordination sphere around Eu^{3+} and its symmetry.[106]

When Eu^{3+} complexes are excited at 395 nm into the $^7F_0 \rightarrow {}^5L_6$ transition of Eu^{3+}, the characteristic line-like emission spectrum of the metal ion is seen (Fig. 6). Different coordination environments lead to slight changes in symmetry and thus fine structure, as addressed above and as can be seen from the spectra in Fig. 6, which indicates that different species are obtained when EDTA coordinates to Eu^{3+} in different protonation states (*i.e.* different pH values). Fig. 6 shows that the coordination environment of Eu^{3+} changed when in contact with EDTA, which agrees with the known fact that EDTA binds Eu^{3+}, and validates our experimental approach.

Fig. 7 supports that the coordination environment of Eu^{3+} changed when in contact with nicotianamine. The differences in emission and excitation spectra between $[Eu^{3+}·(H_2O)_n]^{3+}$ and $[Eu^{3+}–NA·(H_2O)_n]^{3+}$ strongly suggest that Eu and NA are forming a complex because a similar change is observed when Eu^{3+} comes in contact with EDTA, which is known to form a complex. This supports, yet doesn't confirm, that nicotianamine binds Eu^{3+}, as predicted by computation (Section III.B).

From the spectra in Fig. 6 and 7, we can compare and contrast the coordination environments of the Eu^{3+} aqua ion and the Eu^{3+} species bound with NA or $EDTA^{4-}$. The aqua complex spectra are fairly independent of pH, and they show three strong, fairly broad emission peaks corresponding to $^5D_0 \rightarrow {}^7F_J$ (J = 1, 2 and 4) with J = 1 and 4 as the more intense. This is consistent with a species with relatively high symmetry, as would be expected, considering that all binding partners for the Eu^{3+} are water molecules. Substituting a small number of water molecules with either EDTA or NA leads to a decrease in symmetry of the coordination environment around the Eu^{3+} ion, which is principally reflected in the appearance of a fairly intense $^5D_0 \rightarrow {}^7F_0$ transition. The other three peaks show a more resolved fine structure, also consistent with a decrease in symmetry. The changes in relative intensities of these other three transitions, when compared to the aqua complex, are again consistent with a different coordination environment.

III.D. Electronic structure of Eu^{3+}–ligand complexes

To further investigate coordination bonds in $[Eu^{3+}–NA·(H_2O)_n]^{3+}$ complexes, we analyzed their valence MOs, which were calculated with an M06/DKH2-SARC/def2-TZVPP level of theory. The MO diagrams for valence orbitals of the $[Eu^{3+}–NA·(H_2O)_n]^{3+}$ complexes appear in Fig. 8a, and a depiction of their HOMO and LUMO orbitals are shown in Fig. 8b. Fig. S6 in the ESI† shows the MOs and orbitals of the $[Eu^{3+}–EDTA^{4-}·(H_2O)_3]^-$ complex. Thus, in the present paper, we provide a qualitative description of the electronic structure of the previously

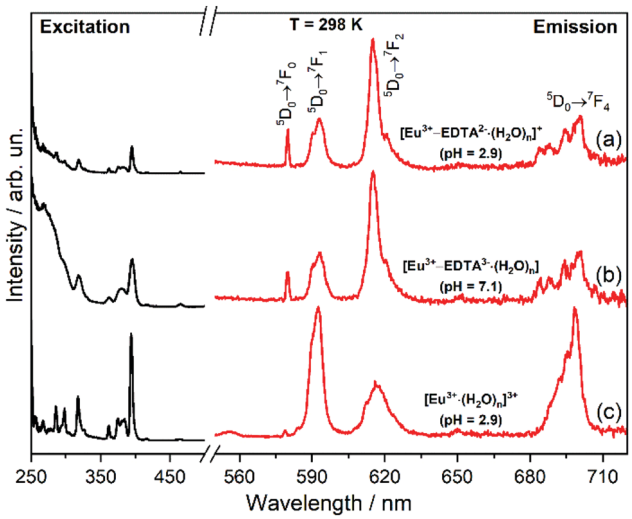

Fig. 6 Excitation (black line, left) and emission (red line, right) spectra of (a) $[Eu^{3+}–EDTA^{2-}·(H_2O)_n]^+$ at pH 2.9, (b) $[Eu^{3+}–EDTA^{3-}·(H_2O)_n]$ at pH 7.1, and (c) $[Eu^{3+}·(H_2O)_n]^{3+}$ complexes in aqueous solution. λ_{exc} = 395 nm.

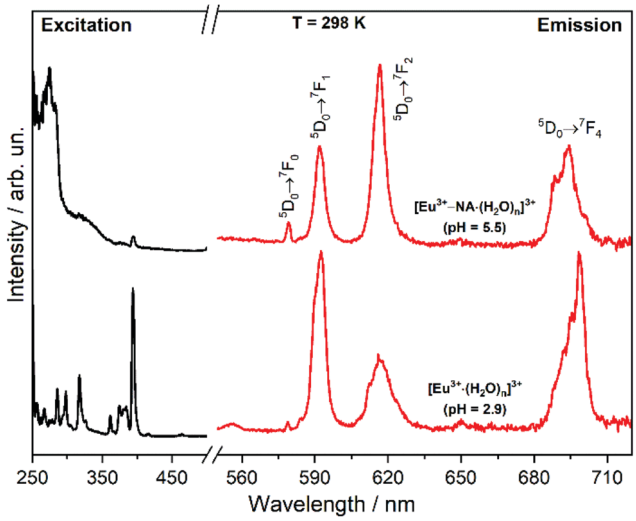

Fig. 7 Excitation (black line, left) and emission (red line, right) spectra of $[Eu^{3+}–NA·(H_2O)_n]^{3+}$ at pH 5.5 (top, λ_{exc} = 285 nm) and $[Eu·(H_2O)_n]^{3+}$ (bottom, λ_{exc} = 395 nm) complexes in aqueous solution.

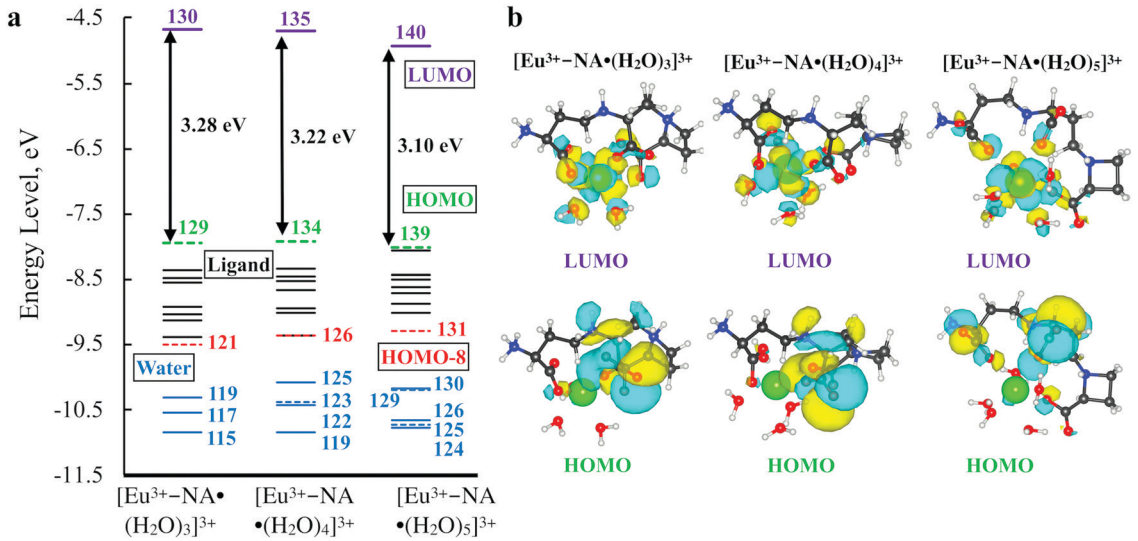

Fig. 8 Valence molecular orbitas (MOs) of the $[Eu^{3+}–NA·(H_2O)_n]^{3+}$ complexes. (a) MO diagrams. (b) HOMO and LUMO orbitals, the orbital wave functions are positive in the yellow regions and negative in the cyan.

unresolved Eu^{3+}–nicotianamine complexes to complement our molecular structure findings (Section III.B).

Fig. 8a shows that the energy levels of MOs in the $[Eu^{3+}–NA·(H_2O)_n]^{3+}$ complexes are qualitatively different, which indicates that having carboxylate groups change from bidentate to monodentate affects not only the number of bound water molecules, but also the electronic structure in all coordination bonds. The lower energies of MOs corresponding to bound water molecules in the $[Eu^{3+}–NA·(H_2O)_3]^{3+}$ complex compared to the bound water MOs in the $[Eu^{3+}–NA·(H_2O)_4]^{3+}$ and $[Eu^{3+}–NA·(H_2O)_5]^{3+}$ complexes indicate that water molecules have higher contribution to binding in the $[Eu^{3+}–NA·(H_2O)_3]^{3+}$ complex. Also, the orbitals corresponding to the ligand are lower in energy in the $[Eu^{3+}–NA·(H_2O)_3]^{3+}$ complex, which indicates that this structure could be energetically favored compared to other nicotianamine complex structures. Moreover, we observe that HOMO–LUMO gaps decrease as the binding conformation favors monodentate binding with more water molecules. All three $[Eu^{3+}–NA·(H_2O)_n]^{3+}$ complexes have HOMO–LUMO gaps larger than that of the $[Eu^{3+}–EDTA^{4-}·(H_2O)_3]^{-}$ complex (2.74 eV, Fig. S6, ESI†), with the $[Eu^{3+}–NA·(H_2O)_5]^{3+}$ complex closest to that of the $[Eu^{3+}–EDTA^{4-}·(H_2O)_3]^{-}$ complex. There is qualitative agreement with the AIMD simulations as well: the Eu–O coordination bond lengths involving monodentate COO^{-} groups (Fig. S3, ESI†) and water molecules (Fig. S5, ESI†) are noticeably more rigid in the $[Eu^{3+}–NA·(H_2O)_3]^{3+}$ and $[Eu^{3+}–NA·(H_2O)_4]^{3+}$ complexes than those in the $[Eu^{3+}–NA·(H_2O)_5]^{3+}$ and $[Eu^{3+}–EDTA^{4-}·(H_2O)_3]^{-}$ complexes.

Although multi-reference calculations are necessary for a more robust validation of Ln^{3+} complexes stabilities,[107–109] we quantified the binding energies of the $[Eu^{3+}–NA·(H_2O)_n]^{3+}$ complexes with respect to the binding energy of the $[Eu^{3+}–EDTA^{4-}·(H_2O)_3]^{-}$ complex (well known to bind Eu^{3+} ions) with an M06/DKH2-SARC/def2-TZVPP level of theory that includes relativistic effects (Section II.A.2). The binding energies were calculated as:

$$\text{Binding energy} = E(Eu^{3+}\text{-ligand}\cdot(H_2O)_n) - E(Eu^{3+}) - E(\text{ligand}) - n\cdot E(H_2O)$$

where the energy of each species was calculated from a single point energy calculation using solution phase coordinates, as described in the Section II.A.2. The three $[Eu^{3+}–NA·(H_2O)_n]^{3+}$ complexes are energetically favored to bind (Table S1, ESI†). Using the binding energy of the $[Eu^{3+}–EDTA^{4-}·(H_2O)_3]^{-}$ complex as the reference point (set to a value of 1), the binding energies of the $[Eu^{3+}–NA·(H_2O)_3]^{3+}$, $[Eu^{3+}–NA·(H_2O)_4]^{3+}$, and $[Eu^{3+}–NA·(H_2O)_5]^{3+}$ complexes are 0.78, 0.81, 0.80, respectively. Thus, binding energy calculations predict that NA at neutral pH will bind Eu^{3+}, but not as strongly as EDTA does in basic conditions.

Unlike the Eu–O length trends observed from AIMD simulations, and qualitative inferences from the MO diagrams, the $[Eu^{3+}–NA·(H_2O)_4]^{3+}$ and $[Eu^{3+}–NA·(H_2O)_5]^{3+}$ complexes have more favorable binding energies than the $[Eu^{3+}–NA·(H_2O)_3]^{3+}$ complex. Also, we observe an inverse trend between HOMO–LUMO gap and binding energies. We plan to do a more thorough thermodynamic stability quantification in the near future, to determine if Eu–NA complexes in water have multiple binding conformations in equilibrium, or to identify which of the three binding conformations is more stable and energetically favored in solution.

IV. Conclusions

This work reports computationally predicted Eu^{3+}–nicotianamine complex structures in solution, which are supported by the fact that the same computational methods and approach were used to replicate the known Eu^{3+}–EDTA complex structure. While our excitation and emission spectroscopy measurements by themselves do not resolve the structure, they confirm that the coordination sphere of Eu^{3+} ions change when in contact with nicotianamine, strongly supporting that the computationally predicted Eu^{3+}–nicotianamine complex is forming. Although knowledge that nicotianamine binds europium does

not determine how plants uptake rare earths from the environment, it strongly supports that phytosiderophores bind lanthanides.

This work also shows that AIMD simulations can be used to accurately predict the structure of lanthanide–ligand complexes in solution, by replicating the structure of the $[Eu^{3+}–EDTA^{4-}\cdot(H_2O)_3]^-$ complex in basic conditions, within 0.05 Å, compared to X-ray fine structure absorption spectroscopy measurements from the literature.[79,80] Paired with the fact that our pseudopotentials and basis sets can accurately predict lanthanide reactivity,[69] a very powerful computational approach allows to properly predict Eu–ligand complex structures in solution, which considers the forming and/or breaking of lanthanide–ligand and lanthanide–solvent coordination bonds. This will be highly useful to efforts in rare earth separation and purification, lanthanide–ligand based medical contrast agents, single molecule magnets, luminescent molecules, and any field in which resolving the structure and reactivity of lanthanides in the atomic scale is relevant.

Conflicts of interest

There are no conflicts to declare.

Acknowledgements

This work was supported by the Vice Presidency for Research and Innovation, and the College of Engineering, of the University of Nevada, Reno. Calculations were performed in Pronghorn, the High Performance Computing cluster of the University of Nevada, Reno. AdBD acknowledges NSF support of this work (CHE-1800392).

References

1 D. Parker and J. A. G. Williams, Getting excited about lanthanide complexation chemistry, *J. Chem. Soc., Dalton Trans.*, 1996, 3613.
2 D. Parker, R. S. Dickins, H. Puschmann, C. Crossland and J. A. K. Howard, Being excited by lanthanide coordination complexes: Aqua species, chirality, excited-state chemistry, and exchange dynamics, *Chem. Rev.*, 2002, **102**, 1977–2010.
3 T. Cheisson and E. J. Schelter, Rare earth elements: Mendeleev's bane, modern marvels, *Science*, 2019, **363**, 489–493.
4 E. Aluicio-Sarduy, N. A. Thiele, K. E. Martin, B. A. Vaughn, J. Devaraj, A. P. Olson, T. E. Barnhart, J. J. Wilson, E. Boros and J. W. Engle, Establishing Radiolanthanum Chemistry for Targeted Nuclear Medicine Applications, *Chem. – Eur. J.*, 2020, **26**, 1238–1242.
5 N. M. Shavaleev, S. V. Eliseeva, R. Scopelliti and J. C. G. Bünzli, Designing simple tridentate ligands for highly luminescent europium complexes, *Chem. – Eur. J.*, 2009, **15**, 10790–10802.
6 E. G. Moore, A. P. S. Samuel and K. N. Raymond, From antenna to assay: lessons learned in lanthanide luminescence, *Acc. Chem. Res.*, 2009, **42**, 542–552.
7 A. de Bettencourt-Dias, in *Luminescence of Lanthanide Ions in Coordination Compounds and Nanomaterials*, ed. A. de Bettencourt-Dias, John Wiley and Sons, Hoboken, 2014, p. 384.
8 P. Martin-Ramos and M. Ramos-Silva, *Lanthanide-Based Multifunctional Materials: From OLEDs to SIMs*, Elsevier, 2018.
9 S. V. Eliseeva and J.-C. G. Bünzli, Lanthanide luminescence for functional materials and bio-sciences, *Chem. Soc. Rev.*, 2010, **39**, 189–227.
10 J. Zhou, J. L. Leaño Jr, Z. Liu, D. Jin, K.-L. Wong, R.-S. Liu and J.-C. G. Bünzli, Impact of lanthanide nanomaterials on photonic devices and smart applications, *Small*, 2018, **14**, 1801882.
11 M. Bettinelli, L. Carlos and X. Liu, Lanthanide-doped upconversion nanoparticles, *Phys. Today*, 2015, **68**, 38–44.
12 *Luminescence of Lanthanide Ions in Coordination Compounds and Nanomaterials*, ed. A. de Bettencourt-Dias, John Wiley and Sons, Hoboken, 2014.
13 J. C. G. Bünzli, in *Luminescence of Lanthanide Ions in Coordination Compounds and Nanomaterials*, ed. A. de Bettencourt-Dias, John Wiley and Sons, Hoboken, 2014, pp. 125–196.
14 E. Deiters, B. Song, A. S. Chauvin, C. D. B. Vandevyver, F. Gumy and J. C. G. Bünzli, Luminescent bimetallic lanthanide bioprobes for cellular imaging with excitation in the visible-light range, *Chem. – Eur. J.*, 2009, **15**, 885–900.
15 S. Faulkner, S. J. A. Pope and B. P. Burton-Pye, Lanthanide complexes for luminescence imaging applications, *Appl. Spectrosc. Rev.*, 2005, **40**, 1–31.
16 J. H. Jia, Q. W. Li, Y. C. Chen, J. L. Liu and M. L. Tong, Luminescent single-molecule magnets based on lanthanides: Design strategies, recent advances and magneto-luminescent studies, *Coord. Chem. Rev.*, 2019, **378**, 365–381.
17 *Lanthanide probes in life, chemical and earth sciences theory and practice*, ed. J.-C. G. Bünzli and G. R. Choppin, Elsevier Science Ltd, Amsterdam, Netherlands, 1990.
18 V. S. Sastri, J. C. Bünzli, V. R. Rao, G. V. S. Rayudu and J. R. Perumareddi, *Modern Aspects of Rare Earths and Their Complexes*, Elsevier Science Ltd, Amsterdam, Netherlands, 2003.
19 S. M. Ramírez-Olvera, L. I. Trejo-Téllez, S. García-Morales, J. A. Pérez-Sato and F. C. Gómez-Merino, Cerium enhances germination and shoot growth, and alters mineral nutrient concentration in rice, *PLoS One*, 2018, **13**, 1–19.
20 G. Tyler, Rare earth elements in soil and plant systems - A review, *Plant Soil*, 2004, **267**, 191–206.
21 J. A. Cotruvo, The Chemistry of Lanthanides in Biology: Recent Discoveries, Emerging Principles, and Technological Applications, *ACS Cent. Sci.*, 2019, **5**, 1496–1506.
22 M. Kovaříková, I. Tomášková and P. Soudek, Rare earth elements in plants, *Biol. Plant.*, 2019, **63**, 20–32.

23 L. Chistoserdova, Lanthanides: New life metals?, *World J. Microbiol. Biotechnol.*, 2016, **32**, 1–7.
24 I. Šola, I. Piantanida, I. Crnolatac and G. Rusak, Europium improves the transport of quercetin through Arabidopsis thaliana, *Biol. Plant.*, 2015, **59**, 554–559.
25 L. J. Daumann, Essential and Ubiquitous: The Emergence of Lanthanide Metallobiochemistry, *Angew. Chem., Int. Ed.*, 2019, **58**, 12795–12802.
26 R. J. Fellows, Z. Wang and C. C. Ainsworth, Europium Uptake and Partitioning in Oat (Avena sativa) Roots as Studied by Laser-Induced Fluorescence Spectroscopy and Confocal Microscopy Profiling Technique, *Environ. Sci. Technol.*, 2003, **37**, 5247–5253.
27 J. L. Gardea-Torresdey, K. J. Tiemann, J. R. Peralta-Videa, J. G. Parsons and M. Delgado, Binding of erbium(III) and holmium(III) to native and chemically modified alfalfa biomass: A spectroscopic investigation, *Microchem. J.*, 2004, **76**, 65–76.
28 J. G. Parsons, J. L. Gardea-Torresdey, K. J. Tiemann, J. H. Gonzalez, J. R. Peralta-Videa, E. Gomez and I. Herrera, Absorption and emission spectroscopic investigation of the phyto-extraction of europium(III) nitrate from aqueous solutions by alfalfa biomass, *Microchem. J.*, 2002, **71**, 175–183.
29 P. Mikołajczak, K. Borowiak and P. Niedzielski, Phytoextraction of rare earth elements in herbaceous plant species growing close to roads, *Environ. Sci. Pollut. Res.*, 2017, **24**, 14091–14103.
30 S. Ding, T. Liang, C. Zhang, Z. Huang, Y. Xie and T. Chen, Fractionation mechanisms of rare earth elements (REEs) in hydroponic wheat: An application for metal accumulation by plants, *Environ. Sci. Technol.*, 2006, **40**, 2686–2691.
31 Z. Chour, B. Laubie, J. L. Morel, Y. Tang, R. Qiu, M. O. Simonnot and L. Muhr, Recovery of rare earth elements from *Dicranopteris dichotoma* by an enhanced ion exchange leaching process, *Chem. Eng. Process*, 2018, **130**, 208–213.
32 J. Saatz, D. Vetterlein, J. Mattusch, M. Otto and B. Daus, The influence of gadolinium and yttrium on biomass production and nutrient balance of maize plants, *Environ. Pollut.*, 2015, **204**, 32–38.
33 S. Lim and S. J. Franklin, Lanthanide-binding peptides and the enzymes that Might Have Been, *Cell. Mol. Life Sci.*, 2004, **61**, 2184–2188.
34 Y. Hibi, K. Asai, H. Arafuka, M. Hamajima, T. Iwama and K. Kawai, Molecular structure of La^{3+}-induced methanol dehydrogenase-like protein in *Methylobacterium radiotolerans*, *J. Biosci. Bioeng.*, 2011, **111**, 547–549.
35 N. A. Fitriyanto, M. Fushimi, M. Matsunaga, A. Pertiwiningrum, T. Iwama and K. Kawai, Molecular structure and gene analysis of Ce^{3+}-induced methanol dehydrogenase of *Bradyrhizobium* sp. MAFF211645, *J. Biosci. Bioeng.*, 2011, **111**, 613–617.
36 T. Nakagawa, R. Mitsui, A. Tani, K. Sasa, S. Tashiro, T. Iwama, T. Hayakawa and K. Kawai, A Catalytic Role of XoxF1 as La^{3+}-Dependent Methanol Dehydrogenase in Methylobacterium extorquens Strain AM1, *PLoS One*, 2012, **7**, 1–7.
37 N. M. Good, M. Fellner, K. Demirer, J. Hu, R. P. Hausinger and N. C. Martinez-Gomez, Lanthanide-dependent alcohol dehydrogenases require an essential aspartate residue for metal coordination and enzymatic function, *J. Biol. Chem.*, 2020, **295**, 8272–8284.
38 C. Liu, F. S. Hong, Y. Tao, T. Liu, Y. N. Xie, J. H. Xu and Z. R. Li, The mechanism of the molecular interaction between cerium(III) and ribulose-1,5-bisphosphate carboxylase/oxygenase (Rubisco), *Biol. Trace Elem. Res.*, 2011, **143**, 1110–1120.
39 S. G. Wildman, Along the trail from Fraction I protein to Rubisco (ribulose bisphosphate carboxylase-oxygenase), *Photosynth. Res.*, 2002, **73**, 243–250.
40 T. D. Sharkey, Discovery of the canonical Calvin–Benson cycle, *Photosynth. Res.*, 2019, **140**, 235–252.
41 R. C. Hider, E. Yoshimura, H. Khodr, N. Von Wirén, S. The, N. Phytologist and N. Nov, Competition or Complementation: The Iron-Chelating Abilities of Nicotianamine and Phytosiderophores, *New Phytol.*, 2004, **164**, 204–208.
42 E. Ahmed and S. J. M. Holmström, Siderophores in environmental research: Roles and applications, *Microb. Biotechnol.*, 2014, **7**, 196–208.
43 S. K. Ghosh, T. Bera and A. M. Chakrabarty, Microbial siderophore – a boon to agricultural sciences, *Biol. Control*, 2020, 104214.
44 J. Leong, Siderophores: Their Biochemistry and Possible Role in the Biocontrol of Plant Pathogens, *Annu. Rev. Phytopathol.*, 1986, **24**, 187–209.
45 M. Takahashi, Y. Terada, I. Nakai, H. Nakanishi, E. Yoshimura, S. Mori and N. K. Nishizawa, Role of nicotianamine in the intracellular delivery of metals and plant reproductive development, *Plant Cell*, 2003, **15**, 1263–1280.
46 L. J. Daumann, P. Werther, M. J. Ziegler and K. N. Raymond, Siderophore inspired tetra- and octadentate antenna ligands for luminescent Eu(III) and Tb(III) complexes, *J. Inorg. Biochem.*, 2016, **162**, 263–273.
47 S. M. Kraemer, J. Xu, K. N. Raymond and G. Sposito, Adsorption of Pb(II) and Eu(III) by oxide minerals in the presence of natural and synthetic hydroxamate siderophores, *Environ. Sci. Technol.*, 2002, **36**, 1287–1291.
48 R. M. Baral and B. K. Kanungo, Experimental and theoretical studies on structure, bonding and luminescence properties of Eu(III) and Tb(III) complexes of a new macrocyclic based 8HQ ligand, *J. Coord. Chem.*, 2019, **72**, 1497–1523.
49 R. J. Abergel, J. A. Warner, D. K. Shuh and K. N. Raymond, Enterobactin protonation and iron release: Structural characterization of the salicylate coordination shift in ferric enterobactin, *J. Am. Chem. Soc.*, 2006, **128**, 8920–8931.
50 R. M. Boiteau, J. B. Shaw, L. Pasa-Tolic, D. W. Koppenaal and J. K. Jansson, Micronutrient metal speciation is controlled by competitive organic chelation in grassland soils, *Soil Biol. Biochem.*, 2018, **120**, 283–291.

51 N. Von Wirén, S. Klair, S. Bansal, J. F. Briat, H. Khodr, T. Shioiri, R. A. Leigh and R. C. Hider, Nicotianamine chelates both Fe(III) and Fe(II) implications for metal transport in plants, *Plant Physiol.*, 1999, **119**, 1107–1114.

52 N. Von Wiren, H. Khodr and R. C. Hider, Hydroxylated phytosiderophore species possess an enhanced chelate stability and affinity for iron(III), *Plant Physiol.*, 2000, **124**, 1149–1157.

53 M. R. Healy, A. S. Ivanov, Y. Karslyan, V. S. Bryantsev, B. A. Moyer and S. Jansone-Popova, Efficient Separation of Light Lanthanides(III) by Using Bis-Lactam Phenanthroline Ligands, *Chem. – Eur. J.*, 2019, **25**, 6326–6331.

54 S. L. Clegg, P. R. Zalupski and G. Dutech, Ion Interaction Models and Measurements of Eu^{3+} Complexation: HEDTA in Aqueous Solutions at 25 °C Containing 1 : 1 Na^+ Salts and Citrate pH Buffer, *Ind. Eng. Chem. Res.*, 2016, **55**, 2083–2096.

55 G. J. Lumetta, B. M. Rapko, P. A. Garza, B. P. Hay, R. D. Gilbertson, T. J. R. Weakley and J. E. Hutchison, Deliberate design of ligand architecture yields dramatic enhancement of metal ion affinity, *J. Am. Chem. Soc.*, 2002, **124**, 5644–5645.

56 B. W. McCann, N. De Silva, T. L. Windus, M. S. Gordon, B. A. Moyer, V. S. Bryantsev and B. P. Hay, Computer-aided molecular design of bis-phosphine oxide lanthanide extractants, *Inorg. Chem.*, 2016, **55**, 5787–5803.

57 R. J. Ellis, D. M. Brigham, L. Delmau, A. S. Ivanov, N. J. Williams, M. N. Vo, B. Reinhart, B. A. Moyer and V. S. Bryantsev, ''Straining'' to Separate the Rare Earths: How the Lanthanide Contraction Impacts Chelation by Diglycolamide Ligands, *Inorg. Chem.*, 2017, **56**, 1152–1160.

58 B. J. Gullekson, A. T. Breshears, M. A. Brown, J. B. Essner, G. A. Baker, J. R. Walensky, A. Paulenova and A. V. Gelis, Extraction of Water and Speciation of Trivalent Lanthanides and Americium in Organophosphorus Extractants, *Inorg. Chem.*, 2016, **55**, 12675–12685.

59 S. Goedecker and M. Teter, Separable dual-space Gaussian pseudopotentials, *Phys. Rev. B: Condens. Matter Mater. Phys.*, 1996, **54**, 1703–1710.

60 C. Hartwigsen, S. Goedecker and J. Hutter, Relativistic separable dual-space Gaussian pseudopotentials from H to Rn, *Phys. Rev. B: Condens. Matter Mater. Phys.*, 1998, **58**, 3641–3662.

61 M. Krack, Pseudopotentials for H to Kr optimized for gradient-corrected exchange-correlation functionals, *Theor. Chem. Acc.*, 2005, **114**, 145–152.

62 G. Lippert, J. Hutter and M. Parrinello, A hybrid Gaussian and plane wave density functional scheme, *Mol. Phys.*, 1997, **92**, 477–488.

63 D. C. Cantu, J. Lee, M. S. Lee, D. J. Heldebrant, P. K. Koech, C. J. Freeman, R. Rousseau and V. A. Glezakou, Dynamic Acid/Base Equilibrium in Single Component Switchable Ionic Liquids and Consequences on Viscosity, *J. Phys. Chem. Lett.*, 2016, **7**, 1646–1652.

64 L. M. Lawson, Daku, Spin-state dependence of the structural and vibrational properties of solvated iron(II) polypyridyl complexes from AIMD simulations: Aqueous [Fe(bpy)3]Cl2, a case study, *Phys. Chem. Chem. Phys.*, 2018, **20**, 6236–6253.

65 L. Ruiz Pestana, N. Mardirossian, M. Head-Gordon and T. Head-Gordon, Ab initio molecular dynamics simulations of liquid water using high quality meta-GGA functionals, *Chem. Sci.*, 2017, **8**, 3554–3565.

66 K. R. Hahn, M. Iannuzzi, A. P. Seitsonen and J. Hutter, Coverage effect of the CO2 adsorption mechanisms on CeO 2(111) by first principles analysis, *J. Phys. Chem. C*, 2013, **117**, 1701–1711.

67 Y. G. Wang, D. Mei, J. Li and R. Rousseau, DFT+U study on the localized electronic states and their potential role during H_2O dissociation and CO oxidation processes on CeO_2(111) surface, *J. Phys. Chem. C*, 2013, **117**, 23082–23089.

68 J. P. Perdew, K. Burke and M. Ernzerhof, Generalized Gradient Approximation Made Simple, *Phys. Rev. Lett.*, 1996, **77**, 3865–3868.

69 J. B. Lu, D. C. Cantu, M. T. Nguyen, J. Li, V. A. Glezakou and R. Rousseau, Norm-Conserving Pseudopotentials and Basis Sets to Explore Lanthanide Chemistry in Complex Environments, *J. Chem. Theory Comput.*, 2019, **15**, 5987–5997.

70 X. Cao and M. Dolg, Valence basis sets for relativistic energy-consistent small-core lanthanide pseudopotentials, *J. Chem. Phys.*, 2001, **115**, 7348–7355.

71 A. Weigand, X. Cao, J. Yang and M. Dolg, Quasirelativistic f-in-core pseudopotentials and core-polarization potentials for trivalent actinides and lanthanides: Molecular test for trifluorides, *Theor. Chem. Acc.*, 2010, **126**, 117–127.

72 R. B. Ross, S. Gayen and W. C. Ermler, Ab initio relativistic effective potentials with spin-orbit operators. V. Ce through Lu, *J. Chem. Phys.*, 1994, **100**, 8145–8155.

73 T. R. Cundari and W. J. Stevens, Effective core potential methods for the lanthanides, *J. Chem. Phys.*, 1993, **98**, 5555–5565.

74 P. J. Hay and W. R. Wadt, Ab initio effective core potentials for molecular calculations. Potentials for the transition metal atoms Sc to Hg, *J. Chem. Phys.*, 1985, **82**, 270–283.

75 M. Dolg and H. Stoll, Pseudopotential Study of the Rare Earth Monohydrides, Monoxides and Monofluorides, *Theor. Chim. Acta*, 1989, **75**, 369–387.

76 M. Dolg, H. Stoll and H. Preuss, Energy-Adjusted Ab Initio Pseudopotentials for the Rare Earth Elements, *J. Chem. Phys.*, 1989, **90**, 1730–1734.

77 X. Cao, J. Zhang, D. Weissmann, M. Dolg and X. Chen, Accurate quantum chemical modelling of the separation of Eu^{3+} from Am^{3+}/Cm^{3+} by liquid-liquid extraction with Cyanex272, *Phys. Chem. Chem. Phys.*, 2015, **17**, 20605–20616.

78 P. W. Huang, C. Z. Wang, Q. Y. Wu, J. H. Lan, G. Song, Z. F. Chai and W. Q. Shi, Theoretical studies on the synergistic extraction of Am^{3+} and Eu^{3+} with CMPO-HDEHP and CMPO-HEH[EHP] systems, *Dalton Trans.*, 2018, **47**, 5474–5482.

79 N. Sakagami, Y. Yamada, T. Konno and K. I. Okamoto, Crystal structures and stereochemical properties of lanthanide(III) complexes with ethylenediamine-*N*,*N*,*N*′,*N*′-tetraacetate, *Inorg. Chim. Acta*, 1999, **288**, 7–16.

80 J. N. Mathur, P. Thakur, C. J. Dodge, A. J. Francis and G. R. Choppin, Coordination modes in the formation of the ternary Am(III), Cm(III), and Eu(III) complexes with EDTA and NTA: TRLFS, 13C NMR, EXAFS, and thermodynamics of the complexation, *Inorg. Chem.*, 2006, **45**, 8026–8035.

81 J. Hutter, M. Iannuzzi, F. Schiffmann and J. Vandevondele, Cp2k: Atomistic simulations of condensed matter systems, *Wiley Interdiscip. Rev.: Comput. Mol. Sci.*, 2014, **4**, 15–25.

82 I. C. Lin, A. P. Seitsonen, I. Tavernelli and U. Rothlisberger, Structure and dynamics of liquid water from ab initio molecular dynamics-comparison of BLYP, PBE, and revPBE density functionals with and without van der Waals corrections, *J. Chem. Theory Comput.*, 2012, **8**, 3902–3910.

83 M. Chen, H. Y. Ko, R. C. Remsing, M. F. Calegari Andrade, B. Santra, Z. Sun, A. Selloni, R. Car, M. L. Klein, J. P. Perdew and X. Wu, Ab initio theory and modeling of water, *Proc. Natl. Acad. Sci. U. S. A.*, 2017, **114**, 10846–10851.

84 S. Grimmel, G. Schoendorff and A. K. Wilson, Gauging the Performance of Density Functionals for Lanthanide-Containing Molecules, *J. Chem. Theory Comput.*, 2016, **12**, 1259–1266.

85 A. Jaoul, G. Nocton and C. Clavaguéra, Assessment of Density Functionals for Computing Thermodynamic Properties of Lanthanide Complexes, *ChemPhysChem*, 2017, **18**, 2688–2696.

86 J. VandeVondele and J. Hutter, Gaussian basis sets for accurate calculations on molecular systems in gas and condensed phases, *J. Chem. Phys.*, 2007, **127**, 114105.

87 S. Grimme, J. Antony, S. Ehrlich and H. Krieg, A consistent and accurate ab initio parametrization of density functional dispersion correction (DFT-D) for the 94 elements H-Pu, *J. Chem. Phys.*, 2010, **132**, 154104.

88 A. Giard, J. S. Filhol, F. Jolibois, F. Cavelier and D. Berthomieu, Prediction of pK_a Using DFT: The Nicotianamine Polyacid Example, *J. Chem. Theory Comput.*, 2016, **12**, 5493–5500.

89 F. Neese, The ORCA program system, *Wiley Interdiscip. Rev.: Comput. Mol. Sci.*, 2012, **2**, 73–78.

90 F. Neese, Software update: the ORCA program system, version 4.0, *Wiley Interdiscip. Rev.: Comput. Mol. Sci.*, 2018, **8**, 4–9.

91 F. Neese, F. Wennmohs, U. Becker and C. Riplinger, The ORCA quantum chemistry program package, *J. Chem. Phys.*, 2020, **152**, 224108.

92 Y. Zhao and D. G. Truhlar, The M06 suite of density functionals for main group thermochemistry, thermochemical kinetics, noncovalent interactions, excited states, and transition elements: Two new functionals and systematic testing of four M06-class functionals and 12 other function, *Theor. Chem. Acc.*, 2008, **120**, 215–241.

93 M. Douglas and N. M. Kroll, Quantum electrodynamical corrections to the fine structure of helium, *Ann. Phys.*, 1974, **82**, 89–155.

94 B. A. Hess, Applicability of the no-pair equation with free-particle projection operators to atomic and molecular structure calculations, *Phys. Rev. A*, 1985, **32**, 756–763.

95 D. A. Pantazis, X. Y. Chen, C. R. Landis and F. Neese, All-electron scalar relativistic basis sets for third-row transition metal atoms, *J. Chem. Theory Comput.*, 2008, **4**, 908–919.

96 F. Weigend and R. Ahlrichs, Balanced basis sets of split valence, triple zeta valence and quadruple zeta valence quality for H to Rn: Design and assessment of accuracy, *Phys. Chem. Chem. Phys.*, 2005, **7**, 3297–3305.

97 D. E. Woon and T. H. Dunning, Gaussian basis sets for use in correlated molecular calculations. I. The atoms boron through neon and hydrogen, *J. Chem. Phys.*, 1988, **90**, 1007–1023.

98 V. Barone and M. Cossi, Quantum calculation of molecular energies and energy gradients in solution by a conductor solvent model, *J. Phys. Chem. A*, 1998, **102**, 1995–2001.

99 N. Mardirossian and M. Head-Gordon, How Accurate Are the Minnesota Density Functionals for Noncovalent Interactions, Isomerization Energies, Thermochemistry, and Barrier Heights Involving Molecules Composed of Main-Group Elements?, *J. Chem. Theory Comput.*, 2016, **12**, 4303–4325.

100 F. E. Jorge, L. S. C. Martins and M. L. Franco, All-electron double zeta basis sets for the lanthanides: Application in atomic and molecular property calculations, *Chem. Phys. Lett.*, 2016, **643**, 84–88.

101 A. Z. de Oliveira, I. B. Ferreira, C. T. Campos, F. E. Jorge and P. A. Fantin, Segmented all-electron basis sets of triple zeta quality for the lanthanides: application to structure calculations of lanthanide monoxides, *J. Mol. Model.*, 2019, **25**, 1–9.

102 D. Aravena, F. Neese and D. A. Pantazis, Improved Segmented All-Electron Relativistically Contracted Basis Sets for the Lanthanides, *J. Chem. Theory Comput.*, 2016, **12**, 1148–1156.

103 F. Neese, F. Wennmohs, A. Hansen and U. Becker, Efficient, approximate and parallel Hartree-Fock and hybrid DFT calculations. A 'chain-of-spheres' algorithm for the Hartree-Fock exchange, *Chem. Phys.*, 2009, **356**, 98–109.

104 N. M. Edelstein, Comparison of the electronic structure of the lanthanides and actinides, *J. Alloys Compd.*, 1995, **223**, 197–203.

105 G. H. Dieke, *Spectra and energy levels of rare earth ions in crystals*, Interscience Publishers, New York, 1968.

106 P. A. Tanner, *Lanthanide luminescence in solids*, Springer Ser. Fluoresc, 2011, vol. 7.

107 J. M. Senegas, G. Bernardinelli, D. Imbert, J. C. G. Bünzli, P. Y. Morgantini, J. Weber and C. Piguet, Connecting terminal carboxylate groups in nine-coordinate lanthanide

podates: Consequences on the thermodynamic, structural, electronic, and photophysical properties, *Inorg. Chem.*, 2003, **42**, 4680–4695.

108 T. B. Emelina, A. Y. Freidzon, A. A. Bagaturyants and V. E. Karasev, Electronic Structure and Energy Transfer in Europium(III)-Ciprofloxacin Complexes: A Theoretical Study, *J. Phys. Chem. A*, 2016, **120**, 7529–7537.

109 Z. Abbas, S. Dasari, M. J. Beltrán-Leiva, P. Cantero-López, D. Páez-Hernández, R. Arratia-Pérez, R. J. Butcher and A. K. Patra, Luminescent europium(III) and terbium(III) complexes of β-diketonate and substituted terpyridine ligands: Synthesis, crystal structures and elucidation of energy transfer pathways, *New J. Chem.*, 2019, **43**, 15139–15152.